

Dynamics analysis and DSP implementation of the Rulkov neuron model with memristive synaptic crosstalk

Yichen Bi(毕毅晨), Jun Mou(牟俊), Herbert Ho-Ching Iu, Nanrun Zhou(周南润), Santo Banerjee, and Suo Gao(高锁)

Citation: Chin. Phys. B, 2026, 35 (**1**): 010504. DOI: 10.1088/1674-1056/ae1728
http://cpb.iphy.ac.cn; http://iopscience.iop.org/cpb

What follows is a list of articles you may be interested in

Dynamical behavior of ring-star neural networks with small-world characteristics

Minglin Ma(马铭磷), Zhiyi Yuan(袁芷依), Umme Kalsoom, Weizheng Deng(邓为政), and Shaobo He(贺少波)
Chin. Phys. B, 2025, 34 (**10**): 100502. DOI: 10.1088/1674-1056/adde39

A novel non-autonomous hyperchaotic map based on discrete memristor parallel connection

Weiping Wu(吴伟平), Mengjiao Wang(王梦蛟), and Qigui Yang(杨启贵)
Chin. Phys. B, 2025, 34 (**5**): 050503. DOI: 10.1088/1674-1056/adb8bc

Fractional-order heterogeneous memristive Rulkov neuronal network and its medical image watermarking application

Dawei Ding(丁大为), Yan Niu(牛炎), Hongwei Zhang(张红伟), Zongli Yang(杨宗立), Jin Wang(王金), Wei Wang(王威), and Mouyuan Wang(王谋媛)
Chin. Phys. B, 2024, 33 (**5**): 050503. DOI: 10.1088/1674-1056/ad322b

A novel hyperchaotic map with sine chaotification and discrete memristor

Qiankun Sun(孙乾坤), Shaobo He(贺少波), Kehui Sun(孙克辉), and Huihai Wang(王会海)
Chin. Phys. B, 2022, 31 (**12**): 120501. DOI: 10.1088/1674-1056/ac8f3a

The dynamics of a memristor-based Rulkov neuron with fractional-order difference

Yan-Mei Lu(卢艳梅), Chun-Hua Wang(王春华), Quan-Li Deng(邓全利), and Cong Xu(徐聪)
Chin. Phys. B, 2022, 31 (**6**): 060502. DOI: 10.1088/1674-1056/ac539a

---

SPECIAL TOPIC — Biophysical circuits: Modeling & applications in neuroscience

Dynamics analysis and DSP implementation of the Rulkov neuron model with memristive synaptic crosstalk

Yichen Bi(毕毅晨)[1], Jun Mou(牟俊)[1], Herbert Ho-Ching Iu[2], Nanrun Zhou(周南润)[3], Santo Banerjee[4], and Suo Gao(高锁)[1,†]

[1] *School of Information Science and Engineering, Dalian Polytechnic University, Dalian* 116034, *China*
[2] *School of Electrical, Electronic and Computer Engineering, The University of Western Australia, Perth* 6009, *Australia*
[3] *School of Electronic and Electrical Engineering, Shanghai University of Engineering Science, Shanghai* 201620, *China*
[4] *Department of Mathematical Sciences, Giuseppe Luigi Lagrange, Politecnico di Torino, Corso Duca degli Abruzzi* 24, *Torino, Italy*

(Received 12 August 2025; revised manuscript received 22 October 2025; accepted manuscript online 24 October 2025)

The human brain is a complex intelligent system composed of tens of billions of neurons interconnected through synapses, and its intricate network structure has consistently attracted numerous scientists to explore the mysteries of brain functions. However, most existing studies have only verified the biological mimicry characteristics of memristors at the single neuron-synapse level, and there is still a lack of research on memristors simulating synaptic coupling between neurons in multi-neuron networks. Based on this, this paper uses discrete memristors to couple dual discrete Rulkov neurons, and adds synaptic crosstalk between the two discrete memristors to form a neuronal network. A memristor-coupled dual-neuron map, called the Rulkov–memristor–Rulkov (R-M-R) map, is constructed to simulate synaptic connections between neurons in biological tissues. Then, the equilibrium points of the R-M-R map are studied. Subsequently, the effect of parameter variations on the dynamic performance of the R-M-R map is comprehensively analyzed using bifurcation diagram, phase diagram, Lyapunov exponent spectrum (LEs), firing diagram, and spectral entropy (SE) complexity algorithms. In the R-M-R map, diverse categories of periodic, chaotic, and hyperchaotic attractors, as well as different states of firing patterns, can be observed. Additionally, different types of state transitions and coexisting attractors are discovered. Finally, the feasibility of the model in digital circuits is verified using a DSP hardware platform. In this study, the coupling principle of biological neurons is simulated, the chaotic dynamic behavior of the R-M-R map is analyzed, and a foundation is laid for deciphering the complex working mechanisms of the brain.

Keywords: Rulkov neuron, discrete memristor, firing patterns, synaptic crosstalk, DSP implementation

PACS: 05.45.Gg, 05.45.Jn

DOI: 10.1088/1674-1056/ae1728 **CSTR:** 32038.14.CPB.ae1728

1. Introduction

Neurons are the basic functional units of the nervous system,[1–3] playing a crucial role in biological information transmission and processing.[4,5] However, the huge number of neurons and complex synaptic connections in the brain make direct experimental observation or physical modeling almost impossible, while mathematical models simplify the study of large-scale neuronal systems by abstractly transforming neuronal biological characteristics into mathematical equations to describe their firing rules.[6,7] Furthermore, the firing behavior of neurons itself has significant nonlinear characteristics: the strength and type of synaptic connections nonlinearly affect neuronal responses, and the interactions between neurons can be simulated by coupling equations to effectively capture the dynamic changes of neuronal firing.[8–10] Therefore, constructing nonlinear mathematical models to simulate neuronal activities such as firing behaviors is of critical significance.[11,12] Studies have shown that the nonlinear adaptive information processing capabilities of neural networks align with the characteristics of chaotic systems, such as sensitivity to initial conditions, dynamic complexity, and nonlinear mapping ability.[13,14] As a result, researchers have proposed numerous models that can simulate the working principles of biological neurons. For example, Boya *et al*. introduced a novel Hopfield neural network (HNN) based on two neurons and found that bursting oscillations emerge with the increase of synaptic weights; additionally, controlling multistability to a single monostable state can realize the normal state of the brain.[15] Liu *et al*. studied the energy method for the firing behaviors of Rulkov neurons based on memristors, and observed mixed-mode firing, bursting firing, and coexisting firing.[16] Compared with other neuron models, discrete neuron models have the advantages of low power consumption, high efficiency, and biological rationality.[17–19] In addition, discrete neuron models can effectively generate chaotic trajectories, which is crucial for understanding the complex dynamic processes of the brain.[20–22] However, existing discrete neuron models still have limitations in simulating the

[†]Corresponding author. E-mail: gaosuo@dlpu.edu.cn

© 2026 Chinese Physical Society and IOP Publishing Ltd. All rights, including for text and data mining, AI training, and similar technologies, are reserved.

synaptic characteristics of real neurons, and many studies only focus on the chaotic characteristics of single neurons. Aiming at these shortcomings, this paper selects the discrete dual-neuron Rulkov model as the research object, which can more realistically present the rich dynamic behaviors of neuron networks.

With the increasing demand for low-power and high-parallel neuromorphic computing, the research on artificial neural networks (ANNs) is shifting from "structural imitation" to "functional biomimetics", with the replication of information exchange between biological neurons being a key focus in the field.[23–25] As the connection hub between neurons, synapses transmit information in the form of chemical or electrical signals and support advanced cognitive functions such as learning and memory through plasticity mechanisms.[26,27] When facing the technical challenges of synaptic simulation, scholars have begun to explore physical devices with memory characteristics, and the concept of memristors, first introduced by Chua in 1971, provides a solution for ANN research.[28] The memristor is a fundamental circuit element describing the relationship between charge and magnetic flux,[29] its resistance value changes with the changes passing through it and it can maintain the altered state after power failure, so it is regarded as an ideal device for simulating neural synapses.[30–32] Meanwhile, memristors can also realize non-volatile state logic operations and brain-inspired neuromorphic computing functions,[33,34] showing wide applications in constructing new types of nonlinear circuits and chaotic circuits. Yu *et al.* studied the dynamical behaviors of memristor synapses among four small neurons, created three memristor-based HNNs, and discovered that the third memristor synaptic HNN can generate hyperchaotic multi-scroll attractors with memristor functions effectively controlling the number of scroll axes, while the designed image encryption scheme exhibits high information entropy and good encryption performance.[35] Hong *et al.* designed a novel circuit using memristors to implement electronic synapses and artificial neurons, laying a solid foundation for the application of memristors in constructing neural network systems.[36] Although the above-mentioned studies have different focuses, the construction of a theoretical system for memristors and biological synapses — ranging from basic simulation to complex cognitive function mapping — still needs further in-depth research.

Linking the synaptic simulation characteristics of memristors with the chaotic nature of the nervous system, their coupling at the nonlinear dynamics level paves a new path for brain-inspired computing research.[37,38] Recently, numerous scholars have investigated the chaotic dynamics of neural networks with memristive coupling. Lu *et al.* constructed a memristive synapse-coupled dual Hindmarsh–Rose (HR) neural network in the context of electrical synapses and external stimuli affecting energy exchange in neuronal fields, revealing nonlinear phenomena, complex electrical activities, and the synchronization characteristics of coupled neurons.[39] Compared with traditional memristors, the locally active memristor (LAM) not only approximates the biological prototype in basic characteristics such as threshold firing and nonlinear dynamics, but also has the advantages of low-power event-driven computing and chaotic optimization.[40,41] Based on this, the LAM coupled with neurons can uncover more complex dynamic behaviors. Mou *et al.* proposed an innovative LAM model and, by applying it to coupled FitzHugh–Nagumo and HR neurons, revealed richer dynamic behaviors that demonstrate potential applications in security or encryption fields.[42] Reference [43] focuses on neural network model design and dynamic analysis. It constructs a large-scale discrete memristive Rulkov ring-star neural network model. By analyzing the network using the spatiotemporal patterns, snapshots, and recurrence plots of nodes, it is found that the network exhibits rich behaviors such as double-well chimera and asynchrony. Additionally, three metrics are used to quantify the influence of memristive coupling strength and initial conditions of memristive Rulkov neurons on network behaviors, providing a basis for state regulation; this also offers insights and references for the research of locally active discrete memristor (LADMs) models. Reference [44], based on the local activity principle, proposes a two-lobe discrete corsage memristor (DCM) model, which features characteristics such as bistability and an odd-symmetric locally active region. By combining the two-lobe DCM with a non-chaotic Rulkov neuron, a DCM-coupled neuron map (DNM) model is constructed. Numerical simulations show that the DNM can generate numerous symmetric attractors; moreover, changing the initial value of the memristor enables the acquisition of offset-boosted coexisting attractors with mono-topology and hybrid-topology. In terms of model design, Ref. [45] constructs a family of DCMs with multiple lobes and odd symmetry, and clarifies the correlation between local activity and edge of chaos of LADMs in the discrete domain. In terms of dynamic analysis, it reveals new phenomena in large-scale networks, such as phase chimera and initial condition-regulated coexisting attractors. In terms of application, a telemedicine encryption scheme is designed, and the security and reliability of this scheme are verified through extensive tests.

However, intricate neural networks with synaptic crosstalk, particularly those coupled by LAMs, remain insufficiently explored.[46] Synaptic crosstalk refers to the mutual influence of signal transmission or functional states between adjacent synapses in a neuronal network, which can occur between chemical synapses or electrical synapses and serve as a key component of dynamic regulation in neural networks.[47] Research on synaptic crosstalk has multifaceted promotional

effects in neuroscience, medicine, and related interdisciplinary fields.[48,49] Hence, studying the dynamical behaviors of neural networks with synaptic crosstalk is necessary. Based on this, Zhang *et al*. innovatively used coupled memristors to simulate synaptic crosstalk, and combined it with heterogeneous HNNs that characterize different brain regions to construct a memristive synaptic crosstalk coupled-HNN (MSC-HNN) model. Through the plasticity of synaptic crosstalk, the model exhibits homogeneous dynamic characteristics globally, while retaining the heterogeneous bifurcation processes and attractors of the internal HNNs. It also leverages the sensitivity of synaptic crosstalk to initial conditions to induce multistability phenomena, ultimately realizing the simulation and research of brain region coupling dynamics in a bionic manner.[50] Li *et al*. constructed a heterogeneous neural network composed of Hindmarsh–Rose neurons and Fitzhugh–Nagumo neurons, using mutually coupled memristors to simulate biological synaptic crosstalk. Through multi-dimensional analysis, they explored the influence of crosstalk intensity on the network's firing patterns (such as the coexistence of periodic firing and chaotic firing) and the synchronous firing of neurons. Essentially, relying on the universality of synaptic crosstalk in the brain, this study reveals the regulatory effect of synaptic crosstalk on neural network firing activities in a bionic research manner, thereby improving the understanding of biological neural function mechanisms.[51] Although the aforementioned studies have explored the role of synaptic crosstalk in neural networks from different perspectives, most of these studies focus on continuous systems, with insufficient attention paid to discrete neural networks. In particular, there are few reports combining the dual-neuron structure with LAM and synaptic crosstalk, which still require further in-depth investigation.

Thus, in this paper, locally active discrete memristors are employed to couple discrete dual Rulkov neurons, and two mutually crosstalked memristors are introduced to form a high-dimensional neural network system. Compared with existing research results, the novel contributions of this paper are summarized as follows.

(a) A high-dimensional Rulkov–memristor–Rulkov (R-M-R) map for studying chaotic dynamic behaviors is constructed by using locally active discrete memristors as synapses to couple discrete dual Rulkov neuron, laying a research foundation for analyzing neural information processing mechanisms and developing brain-inspired intelligent algorithms.

(b) By considering parameters such as crosstalk intensity, the rich dynamic behaviors displayed in the R-M-R map are studied, which enriches the understanding of the mechanism of synaptic crosstalk in neuromorphic systems.

(c) Experimental testing of the pseudo-randomness of the R-M-R map was carried out on a DSP platform, and the hardware viability is verified, providing interdisciplinary technical verification for the engineering applications of chaos theory in fields such as neuromorphic computing and encrypted communication.

The remaining parts of this paper are structured as follows. The structure and characteristics of memristors are introduced in Section 2. In Section 3, a memristor-coupled neuron model is established, and the equilibrium points of the R-M-R map are subjected to analysis. In Section 4, dynamic studies are conducted by examining phase diagram, BD, Lyapunov exponent spectrum (LEs), and spectral entropy (SE) complexity that emerge with varying parameters. The implementation of this map on a DSP hardware platform is illustrated in Section 5. Finally, the research findings are summarized, and several conclusions are drawn.

2. Locally active discrete memristor

In this section, the mathematical model of the LAM proposed by Lai *et al*.[52] is introduced. The feasibility of the memristor is verified by the pinched hysteresis loop. The nonvolatile and locally active characteristics of the memristor are analyzed through the power-off plot (POP) and DC V–I plot.

2.1. Mathematical model of a memristor

The discrete memristor model proposed by Lai *et al*. combines practical advantages with model characteristics: it has high anti-interference capability, low fabrication and control costs, and simple application adaptability. Additionally, relying on its local activity property, it can actively amplify weak signals and is suitable for scenarios such as brain-inspired simulations. Essentially, memristors are nonlinear components with memory functions, which is highly consistent with the "strong nonlinear feedback of state variables on their own evolution" exhibited by the cubic term in the model. Furthermore, the cubic term balances complexity and solvability — it avoids the excessive complexity caused by higher-order terms or the linear limitations of lower-order terms while accurately reproducing the memory and nonlinear characteristics of the device. Meanwhile, the model has clear physical interpretability: the state variable φ_n can describe the dynamic characteristics of magnetic flux, and the sine function in the current equation can reflect the nonlinear conductivity modulation mechanism. In summary, this discrete memristor model is adopted in this study.

$$\begin{cases} i_n = W(\varphi_n)v_n = \sin(\varphi_n)v_n, \\ \varphi_{n+1} = -a\varphi_n^3 + b\varphi_n - cv_n, \end{cases} \tag{1}$$

where i_n denotes the output current, v_n denotes the input voltage, φ_n is the magnetic flux, and $W(\varphi_n)$ is the memductance. Using the voltage–current characteristics of the memristor,

these parameters are calibrated. By adjusting the control parameters b, c and a of the discrete memristor to fit the measured v_n–i_n curve, the parameters are finally determined as $b = 1.1$, $c = 0.1$, and $a = 0.1$. These parameters can accurately reflect the dynamic behavior of the memristor. Here, the discrete magnetic flux variable φ_n can take either positive or negative values. Its value is determined by the history of voltage excitation and the evolution of the memristor internal state. A negative value of φ_n is a key indicator that the memristor "remembers" the reverse voltage excitation. Together with its positive state, it forms a complete memory cycle: positive values record the history of forward voltage action, while negative values record the history of reverse voltage action. This ability to record bidirectional states enables the memristor to adjust its current electrical response based on the alternating excitation of past positive and negative voltages, which serves as the core foundation for its implementation of functions such as logic operations and data storage.

Basic properties and dynamic behaviors of discrete memristor are investigated by applying $V_n = A\sin(\omega_n)$. Setting the frequency $\omega = 0.1$, 0.2, 0.4, and 3 successively, and fixing $A = 1.5$. The voltage–current (v_n–i_n) curve is presented in Fig. 1(a). As can be observed from Fig. 1(a), the area of the pinched hysteresis loops decreases as ω increases. The memristor turns into a linear resistor at $\omega = 3$. Additionally, in Fig. 1(b), with ω fixed at 0.2, the pinched hysteresis loop of the memristor consistently intersects the origin and manifests an "8"-shaped feature as the voltage amplitude increases. These findings verify that the memristor model exhibits memory characteristics.

Comparing this discrete memristor model with continuous memristors in neuromorphic applications can more clearly highlight the advantages of this model in research. As shown in Table 1, the comparison is conducted from four core indicators crucial for neuromorphic applications: synaptic weight update efficiency, hardware implementation feasibility, temporal resolution adaptability, and the robustness of weight updates.

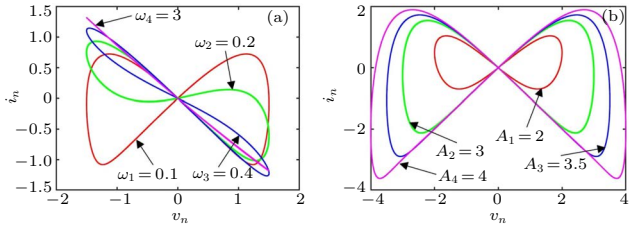


Fig. 1. The pinched hysteresis of the discrete memristor. (a) $A = 1.5$, (b) $\omega = 0.2$.

Table 1. Comparison of continuous and discrete memristors in neuromorphic applications.

Performance indicator	Characteristics of continuous memristors	Characteristics of discrete memristors	Advantages of the discrete model
Synaptic weight update efficiency	×	✓	Fewer calculation steps, shorter single weight update time, suitable for parallel needs of large-scale synaptic networks.
Hardware implementation difficulty and compatibility	×	✓	Low hardware design barrier, high stability, easy integration with neuromorphic chip digital control modules, reducing development costs.
Time resolution adaptability	×	✓	Covers multi-scale time signal processing in neuromorphic applications, boosting system universality.
Robustness of weight update	×	✓	Ensures accurate weight update in complex electromagnetic environments without extra anti-interference design, enhancing neuromorphic system reliability.

2.2. Nonvolatility and local activity

If the POP of the memristor has two or more intersection points with the x-axis at negative slopes, the memristor exhibits non-volatility. Setting $v_n = 0$ in Eq. (1) yields

$$\varphi_{n+1} - \varphi_n = -0.1\varphi_n^3 + 0.1\varphi_n. \tag{2}$$

After obtaining Eq. (2), the POP of the memristor is shown in Fig. 2(a). The evolution direction of φ_n, as indicated by the arrows in the figure, follows the no-backtracking rule of the non-volatile memristors. The figure indicates that the POP of the memristor presents two negative slopes and one positive slope. The three points of intersection with the x-axis are Q_1, Q_2, and Q_3, respectively, indicating that there exist three fixed points in the memristor. Q_1 and Q_3 represent two asymptotically stable fixed points exhibiting negative slopes, while Q_2 is an unstable fixed point with a corresponding positive slope. For different initial states φ_n of the memristor, the following are the limit states:

$$\varphi_{(\infty)} = \begin{cases} \varphi(Q_1) = -1, & \text{if } \varphi_{(0)} < 0, \\ \varphi(Q_2) = 0, & \text{if } \varphi_{(0)} = 0, \\ \varphi(Q_3) = 1, & \text{if } \varphi_{(0)} > 0, \end{cases} \tag{3}$$

which indicates two stable memductances

$$\begin{cases} G(Q_1) = \sin(-1) = -0.8415, & \varphi_{(0)} < 0, \\ G(Q_3) = \sin(1) = 0.8415, & \varphi_{(0)} > 0. \end{cases} \tag{4}$$

The locally active characteristics can be derived from the DC V–I characteristic curve. In Eq. (1), when setting $\varphi_{n+1} = \varphi_n$, it can then be deduced that

$$\begin{cases} V = -\frac{a}{c}\varphi_n^3 + \frac{b-1}{c}\varphi_n, \\ I = W(\varphi_n)V = \sin(\varphi_n)(-\frac{a}{c}\varphi_n^3 + \frac{b-1}{c}\varphi_n). \end{cases} \tag{5}$$

Here, V and I represent DC voltage and DC current, respectively. The locally active characteristic can be confirmed by the red line with a negative slope in the DC V–I diagram plotted in Fig. 2(b), indicating that this memristor is a LAM.

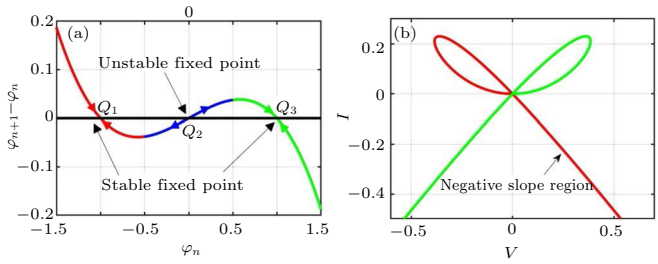


Fig. 2. (a) Power-off plot and (b) DC V–I.

3. The R-M-R model description

This section provides an overview of the discrete Rulkov neuron model,[53] with synapses simulated using the memristor model formulated in Eq. (1). By introducing synaptic crosstalk between the two memristors to simulate the synaptic crosstalk between Rulkov neurons, a six-dimensional discrete memristive synaptically coupled neuron model is constructed.

3.1. Rulkov neuron description

The Rulkov neuron map model is a representative model in the discrete domain, which can demonstrate the nonlinear dynamic behavior and biological characteristics of neurons. This neuron map model is designed to simulate the firing behavior of biological neurons. The two-dimensional discrete Rulkov neuron model can be expressed as

$$\begin{cases} x_{n+1} = \dfrac{\gamma}{(1+x_n)^2} + y_n, \\ y_{n+1} = y_n - \mu(x_n - \sigma), \end{cases} \tag{6}$$

where x_n denotes the fast excitatory variable and y_n represents the slow recovery variable. Within this neuron, σ signifies the external influence. μ and γ serve as control parameters.

Based on the discrete Rulkov neuron, coupling via the proposed memristor can simulate the actual connections of neurons. Therefore, two locally active discrete memristors are added between two 2D Rulkov neurons to perform synaptic simulation. The coupling model of neurons is shown in Eq. (7), where x_n and z_n are the state variables of the Rulkov neuron model, and f_n and g_n are equivalent to the memristor models in Eq. (1).

$$\begin{cases} x_{n+1} = \dfrac{\gamma}{1+(x_n)^2} + y_n - k(\sin(g_n) + b_1 \sin(f_n))(x_n - z_n), \\ y_{n+1} = y_n - \mu(x_n - \sigma), \\ z_{n+1} = \dfrac{\gamma}{1+(z_n)^2} + w_n + k(\sin(f_n) + b_2 \sin(g_n))(x_n - z_n), \\ w_{n+1} = w_n - \mu(z_n - \sigma), \\ f_{n+1} = h(-af_n^3 + bf_n) + (x_n - z_n), \\ g_{n+1} = h(-ag_n^3 + bg_n) + (x_n - z_n). \end{cases} \tag{7}$$

Table 2. The meanings and value ranges of the parameters in the R-M-R map.

Parameters	Physical meaning	Value range
γ	Rulkov neuron parameter	(–7.56, 7.2)
k	Coupling parameter between neurons	(–0.3, 0.31)
b_1	Synaptic crosstalk	(–8.18, 5.72)
μ	Rulkov neuron parameter	(0, 0.666)
σ	Rulkov neuron parameter	(–5.2, 7.2)
b_2	Synaptic crosstalk	(–8.18, 7.22)
h	Resistor related parameter	(–0.14, 0.33)

The relevant parameters of the R-M-R map are shown in Table 2. The topological structure of this model is shown in Fig. 3. This figure presents a brain-inspired system architecture where a memristor-based artificial synapse connects two Rulkov neurons, which is used to simulate the process of signal transmission between neurons via synapses in the biological nervous system. The core lies in utilizing the memristor to implement the function of the artificial synapse and construct a neuromorphic system. Among them, b_1 and b_2 represent synaptic crosstalk, which denotes the signal interference inside the artificial synapse.

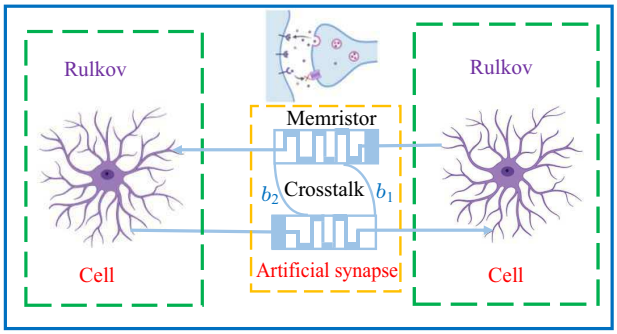


Fig. 3. Discrete memristor-coupled dual Rulkov neurons topology.

The parameters are set as $\gamma = -4$, $k = 0.1$, $b_1 = 0.1$, $\sigma = 1.35$, $b_2 = 0.1$, $h = 0.11$, $a = 0.1$, $b = 1.1$, and the initial values are (0.1, 0.1, 0, 0.1, 0, 0). When $\mu = 0.15$, the R-M-R map exhibits LE1 = 0.99837, LE2 = 0.561382, LE3 = −0.551075, LE4 = −0.995228, LE5 = −7.79386, and LE6 = −9.66477. It is obvious that both values of the Lyapunov exponents are above zero, indicating that the R-M-R map has a hyperchaotic attractor. The hyperchaotic attractors projected onto different planes are shown in Figs. 4(a)–4(c). In the 3D plane, the attractor exhibits a complex spatial structure, indicating that there are intertwined dynamical characteristics among the three variables. The 2D projections in Figs. 4(b) and 4(c) reveal the "shadow" of this 3D chaos, where the point distribution is dense and non-repetitive, lacking simple periodicity. When $\mu = 0.66$, the LEs of the map are LE1 = 0.820195, LE2 = 0.478559, LE3 = −0.240178, LE4 = −0.710883, LE5 = −5.69068, and LE6 = −7.36594. At this point, the system still exhibits a hyperchaotic attractor, as shown in Figs. 4(d)–4(f). Compared with the case when $\mu = 0.15$, the 3D plane presents a completely different spatial

morphology, which indicates that the parameter μ can regulate the dynamical characteristics of the system. The projection in Fig. 4(e) shows a structure with a central hollow and a spiral-like point distribution, while the projection in Fig. 4(f) becomes more scattered. These changes demonstrate that μ modifies the shape, range of the attractor, and the interactions between variables, highlighting that parameter variations can significantly alter the hyperchaotic dynamical properties. This provides intuitive insights into understanding the richness of the system and its sensitivity to parameters.

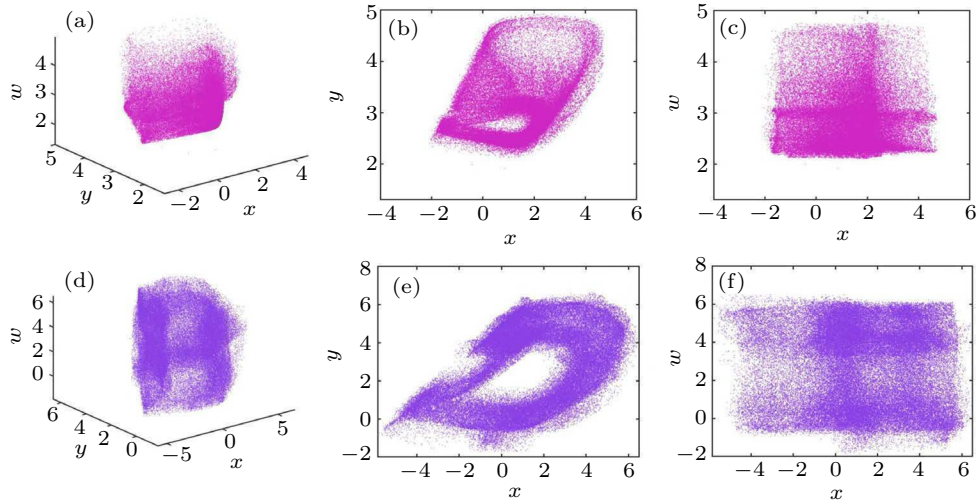


Fig. 4. Hyperchaotic attractors in different planes: (a) x–y–w plane with $\mu = 0.15$, (b) x–y plane with $\mu = 0.15$, (c) x–w plane with $\mu = 0.15$, (d) x–y–w plane with $\mu = 0.66$, (e) x–y plane with $\mu = 0.66$, (f) x–w plane with $\mu = 0.66$.

3.2. Kaplan–Yorke dimension

The Kaplan–Yorke dimension is a crucial concept in the theory of dynamical systems, used to characterize the geometric and dynamical properties of complex systems. In this paper, the Kaplan–Yorke dimension is employed to further verify hyperchaos.

Kaplan-Yorke dimension:

$$D_{\mathrm{KY}} = j + \frac{1}{|\mathrm{LE}_{j+1}|}\sum_{i=1}^{j}\mathrm{LE}_i, \tag{8}$$

where j represents the largest integer that satisfies a specific condition. This condition is: after sorting the Lyapunov exponents (LEs) in descending order, the sum of the first j Lyapunov exponents is greater than or equal to 0, that is, $\sum_{i=1}^{j}\mathrm{LE}_i \geq 0$; and the sum of the first $j+1$ Lyapunov exponents is less than 0, i.e., $\sum_{i=1}^{j+1}\mathrm{LE_i} < 0$. Here, LE_i represents the i-th Lyapunov exponent.

Fix $(\gamma,\ k,\ b_1,\ \sigma,\ b_2,\ h,\ a,\ b) = (-4, 0.1,\ 0.1,\ 1.35,\ 0.1,\ 0.11,\ 0.1,\ 1.1)$ and $(x,\ y,\ z,\ w,\ f,\ g) = (0.1, 0.1, 0, 0.1, 0, 0)$. When $\mu = 0.15$, the Lyapunov exponents sorted in descending order are LE = (0.99837, 0.561382, −0.551075, −0.995228, −7.79386, −9.66477). It is verified that neither $j = 2$ nor $j = 3$ satisfies the conditions, and $j = 4$ also fails to meet the requirements. Specifically, the sum of the first 3 exponents is positive, while the sum becomes sharply negative after including the 4th exponent. Therefore, only $j = 3$ satisfies the core condition that the sum of the first j terms is ≥ 0 and the sum of the first $j+1$ terms is as close as possible to but less than 0, resulting in $D_{\mathrm{KY}} = 4.0135$. With other conditions unchanged.

When $\mu = 0.66$ alone, the Lyapunov exponents sorted in descending order are (0.820195, 0.478559, −0.240178, −0.710883, −5.69068, −7.36594). The calculated Kaplan–Yorke dimension is approximately 4.489. Combining the Kaplan–Yorke dimension with the specific distribution of Lyapunov exponents, it can be concluded that the system is a hyperchaotic system. In actual judgment, it is necessary to combine the specific distribution of the system's dimension and Lyapunov exponents. D_{KY} is an auxiliary indicator and needs to be used in combination with other chaos criteria.

3.3. Equilibrium point analysis

The analysis and calculation of equilibrium points in chaotic systems are important components of the qualitative analysis methods for chaotic mechanisms. For a discrete map at an equilibrium, it satisfies $x_{n+1} = x_n$, indicating that the state variables of the system remain invariant under time evolution or iteration. Therefore, according to Eq. (7), the general mathematical expression for the equilibrium points of the map is obtained as

$$\begin{cases} x^* = \frac{\gamma}{1+(x^*)^2} + y^* - k(\sin(g^*) + b_1\sin(f^*))(x^* - z^*), \\ y^* = y^* - \mu(x^* - \sigma), \\ z^* = \frac{\gamma}{1+(z^*)^2} + w^* + k(\sin(f^*) + b_2\sin(g^*))(x^* - z^*), \\ w^* = w^* - \mu(z^* - \sigma), \\ f^* = h(-a(f^*)^3 + bf^*) + (x^* - z^*), \\ g^* = h(-a(g^*)^3 + bg^*) + (x^* - z^*). \end{cases} \tag{9}$$

Case 1: $x \neq \sigma$ and $z \neq \sigma$, Eq. (9) does not admit an exact analytical solution, indicating that the R-M-R map has no equilibrium points. In this case, the attractor generated by the R-M-R

map is a hidden attractor. Case 2: The solution to Eq. (9) leads to $x=z=\sigma$, $y=w=(\sigma^3+\sigma-\gamma)/(1+\sigma^2)$. Since the state variables f and g each have two solutions, the R-M-R map corresponds to two distinct sets of equilibrium points:

$$\left\{\begin{array}{l} P_1=\left\{\begin{array}{l}(x,y,z,w,f,g)\\ x=z=\sigma, y=w=(\sigma^3+\sigma-\gamma)/(1+\sigma^2),\\ f=g=((hb-1)/ah)^{0.5};\end{array}\right\}\\ P_2=\left\{\begin{array}{l}(x,y,z,w,f,g)\\ x=z=\sigma, y=w=(\sigma^3+\sigma-\gamma)/(1+\sigma^2),\\ f=g=0;\end{array}\right\}\end{array}\right. \tag{10}$$

the Jacobi matrix of the R-M-R map is as follows:

$$J=\begin{bmatrix} A & 1 & B & 0 & 0 & 0\\ -\mu & 1 & 0 & 0 & 0 & 0\\ C & 0 & D & 1 & 0 & 0\\ 0 & 0 & -\mu & 1 & 0 & 0\\ 1 & 0 & -1 & 0 & h(-3af^2+b) & 0\\ 1 & 0 & -1 & 0 & 0 & h(-3ag^2+b)\end{bmatrix}, \tag{11}$$

the characteristic polynomial of Eq. (11) is

$$\begin{aligned} P(\lambda) &= \det(E\lambda-J)\\ &= \left(h(-3af^2+b)-\lambda\right)\left(h(-3ag^2+b)-\lambda\right)\\ &\quad (A\mu+B\mu-A\lambda-B\lambda-2\lambda\mu+2A\lambda^2\\ &\quad -A\lambda^3+2B\lambda^2-B\lambda^3+2\mu\lambda^2+\mu^2+\lambda^2-2\lambda^3\\ &\quad +\lambda^4+AB-CD-2AB\lambda+2CD\lambda\\ &\quad -A\mu\lambda-B\mu\lambda+AB\lambda^2-CD\lambda^2)=0, \end{aligned} \tag{12}$$

where

$$\left\{\begin{array}{l} A=-k(\sin(g)+b_1\sin(f))-(2\gamma\sigma)/(\sigma^2+1)^2,\\ B=k(\sin(g)+b_1\sin(f)),\\ C=k(\sin(f)+b_2\sin(g)),\\ D=-k(\sin(f)+b_2\sin(g))-2\gamma\sigma/(\sigma^2+1)^2,\end{array}\right. \tag{13}$$

the parameters of the R-M-R map were set to (σ, γ, h, b, a, k, μ) = (1.35, −4, 0.3, 4, 0.1, 0, 0.1). Substituting the values of the parameters into Eq. (12), two different characteristic equations can be obtained:

$$\left\{\begin{array}{l} P_1(\lambda)=\left((5\lambda-3)^2(50\lambda^2-118\lambda+73)^2\right)/62500=0,\\ P_2(\lambda)=\left((5\lambda-6)^2(50\lambda^2-118\lambda+73)^2\right)/62500=0.\end{array}\right. \tag{14}$$

The necessary and sufficient condition for the stability of a discrete system is that the modulus of all eigenvalues is strictly less than 1. As long as there is at least one eigenvalue with a modulus greater than 1, the system is unstable. From this, it can be seen that the solutions corresponding to $P_1(\lambda)$ are $\lambda_{11}=3/5$, $\lambda_{12}=3/5$, $\lambda_{13}=(59+13\mathrm{i})/50$, $\lambda_{14}=(59+13\mathrm{i})/50$, $\lambda_{15}=(59-13\mathrm{i})/50$ and $\lambda_{16}=(59-13\mathrm{i})/50$. Here, $|\lambda_{11}|<1$, $|\lambda_{12}|<1$ while $|\lambda_{13}|>1$, $|\lambda_{14}|>1$, $|\lambda_{15}|>1$, and $|\lambda_{16}|>1$. Therefore, in this case, the map is unstable. The real solution corresponding to $P_2(\lambda)$ is $\lambda_{21}=6/5$, $\lambda_{22}=6/5$ and the complex solutions are the same as those of $P_1(\lambda)$, so the map remains unstable. In conclusion, in both cases, the R-M-R map exhibits unstable equilibrium points.

4. Dynamical analysis

In this section, by changing different parameters, the dynamical properties of the R-M-R map are investigated through phase diagrams, BD, LEs, firing patterns, coexisting phenomena, state transitions, and complexity.

4.1. Influences of different parameters on the R-M-R map

4.1.1. The variation of coupling parameter k

The initial values of the R-M-R map are set to (0.1, 0.1, 0, 0.1, 0, 0), and the parameters are set to $\gamma=-4$, $b_2=0.1$, $b_1=0.1$, $\sigma=1.35$, $\mu=0.15$, and $h=0.11$. The BD and corresponding LEs when $k\in(-0.3,0.31)$ are shown in Fig. 5.

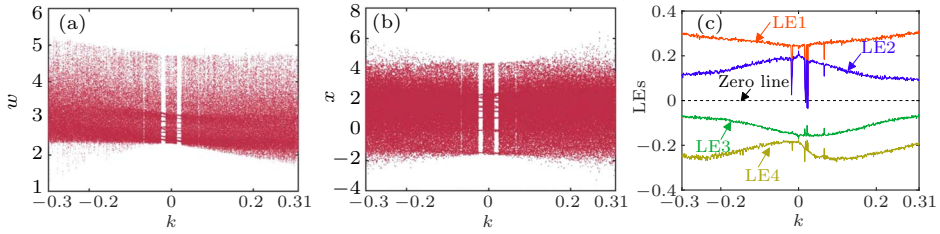


Fig. 5. Dynamical characteristics with $k\in[-0.3,0.31]$. (a) The BD in the k–w plane. (b) The BD in the k–x plane. (c) LEs.

Since the last two Lyapunov exponents are relatively small negative numbers, only LE1, LE2, LE3, and LE4 are plotted for the sake of clarity. This approach runs throughout the following analysis. Within this parameter range, the map undergoes the process of hyperchaos→period→hyperchaos→period→hyperchaos. In the hyperchaotic regimes, there are consistently two positive Lyapunov exponents. When finally entering the hyperchaotic state, multiple periodic windows can be observed, and each periodic window undergoes period-doubling bifurcations, transitioning from a stable period to an unstable period. This implies that in the chaotic region, there not only exists chaotic motion but also multiple unstable periodic orbits. Figure 6 displays attractors in different planes for various values of k.

4.1.2. The variation of coupling parameter γ

The dynamic properties of the R-M-R map are also changed by variations in the neuronal parameter γ. Setting

$k = 0.1$, $b_1 = 0.1$, $b_2 = 0.1$, $\mu = 0.15$, $\sigma = 1.35$, $h = 0.11$, and the initial values are set as (0.1, 0.1, 0, 0.1, 0, 0). As shown in Figs. 7(a) and 7(b), the BD in different planes is presented when $\gamma \in (-5.5, -2.4)$.

It is clearly observable that the LEs of the R-M-R map completely correspond to the BD. From the BD, when $\gamma = -5.21$, the R-M-R map undergoes an inverse period-doubling bifurcation, transitioning from a hyperchaotic state to a periodic state, and then experiences multiple such state transitions. When $\gamma = -2.9$, the R-M-R map again enters a periodic state from a chaotic state through a tangent bifurcation. Within the range of $(-5.5, -2.4)$, it can be seen from the LEs that there are many transitions between hyperchaos and chaos, as well as a large number of periodic windows.

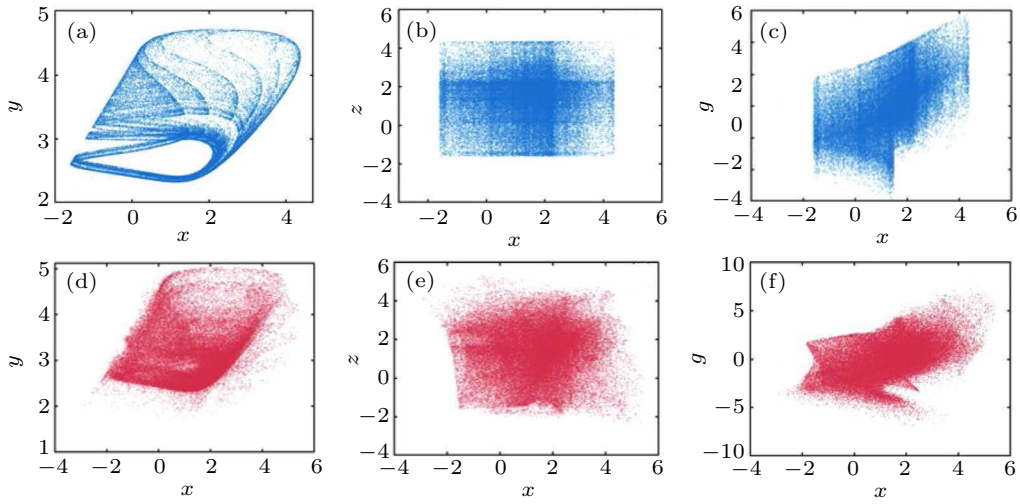


Fig. 6. Attractors with different parameters k in different phases: (a) x–y plane, $k = 0$; (b) x–z plane, $k = 0$; (c) x–g plane, $k = 0$; (d) x–y plane, $k = 0.2$; (e) x–z plane, $k = 0.2$; (f) x–g plane, $k = 0.2$.

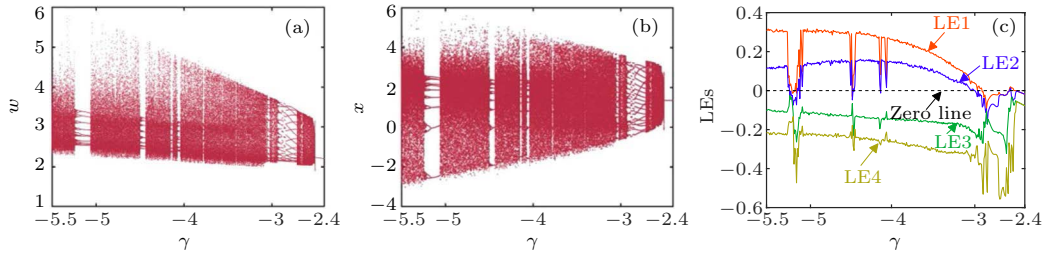


Fig. 7. Dynamical characteristics change with the variation of γ. (a) The BD in the γ–w plane when $\gamma \in (-5.5, -2.4)$. (b) The BD in the γ–x plane when $\gamma \in (-5.5, -2.4)$. (c) The LEs for $\gamma \in (-5.5, -2.4)$.

The BD and LEs in Fig. 8 indicate that when $\gamma \in (-2.4, 7.2)$, the R-M-R map directly enters a hyperchaotic state through period-doubling bifurcation. Moreover, the BD shows obvious discontinuous behaviors. When the parameter γ changes to a specific value, the stable state of the neuron model undergoes a sudden change instead of a gradual transition. Near the discontinuous points, the neuron model is highly sensitive to small changes in the parameter γ; a tiny adjustment of the parameter may lead to a significant change in the neuron state.

However, in the parameter intervals far from the discontinuous points, the neuron state is relatively stable. This characteristic helps neurons in complex biological environments not only to respond quickly to important external stimuli but also to maintain stable activity patterns under normal circumstances.

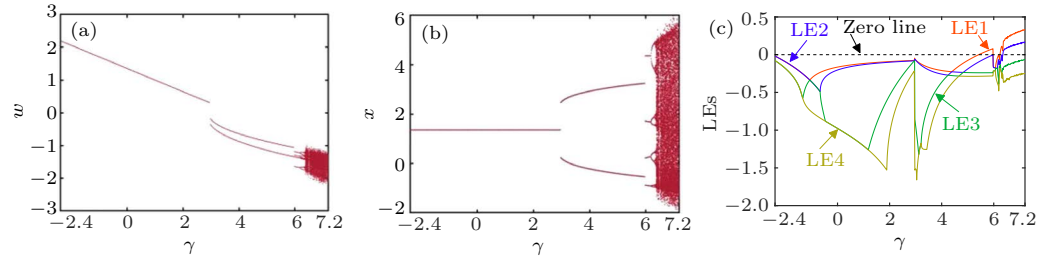


Fig. 8. Dynamical characteristics change with the variation of γ. (a) The BD in the γ–w plane when $\gamma \in (-2.4, 7.2)$. (b) The BD in the γ–x plane when $\gamma \in (-2.4, 7.2)$. (c) The LEs for $\gamma \in (-2.4, 7.2)$.

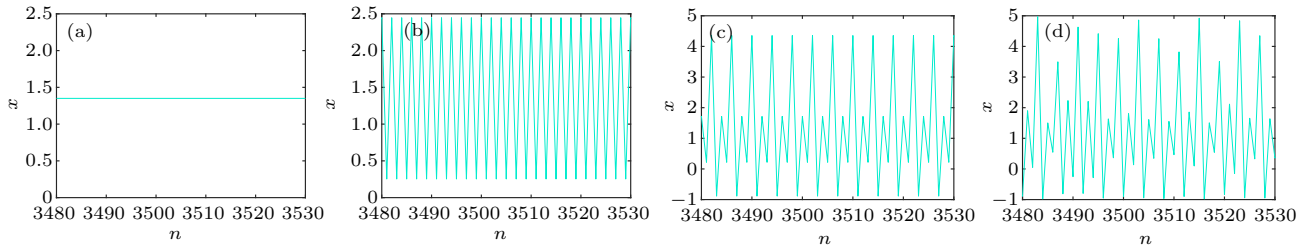


Fig. 9. The firing pattern of γ at the discontinuous point. (a) Quiescent state as $\gamma = 2.94$; (b) periodic firing state as $\gamma = 2.96$; (c) bursting periodic firing state as $\gamma = 5.98$; (d) chaotic firing state as $\gamma = 6.4$.

When $\gamma = 2.94$, the map is in a resting state. As shown in Fig. 9(a), in clinical research, resting-state EEG rhythms are typically recorded from the patient's scalp over a short period — specifically several minutes — under both eyes-closed and eyes-open conditions.[54] Figures 9(b) and 9(c), respectively, show the periodic discharge patterns under different values of γ. In clinical EEG, periodic discharges essentially refer to brain electrical activity with regularly repeating waveform patterns. If the discharges are physiological periodic rhythms, the brain is mostly in a state of relaxed rest or light sleep; if the discharges are pathological periodic rhythms, the brain may be in a state of abnormal electrical activity.[55] When $\gamma = 6.4$, the map exhibits chaotic discharge as shown in Fig. 9(d). Chaotic discharge is divided into physiological chaotic discharge and pathological chaotic discharge: physiological chaos serves as the basis for normal brain function, while in clinical practice the focus lies on pathological chaotic abnormalities, which are often associated with intense abnormal electrical activity during the acute phase of diseases.[56]

In conclusion, the discontinuous behaviors in the BD provide important clues and a theoretical basis for in-depth understanding of the dynamic characteristics of neurons, the mechanisms of neural information processing, and the occurrence and development of nervous system diseases.

The typical dynamic behaviors of the corresponding firings of the map are shown in Fig. 10. In the periodic state, phase trajectories appear as state points and state loops. When in chaotic and hyperchaotic states, attractors exhibit certain structure, and distinct changes are evident in the firing diagrams.

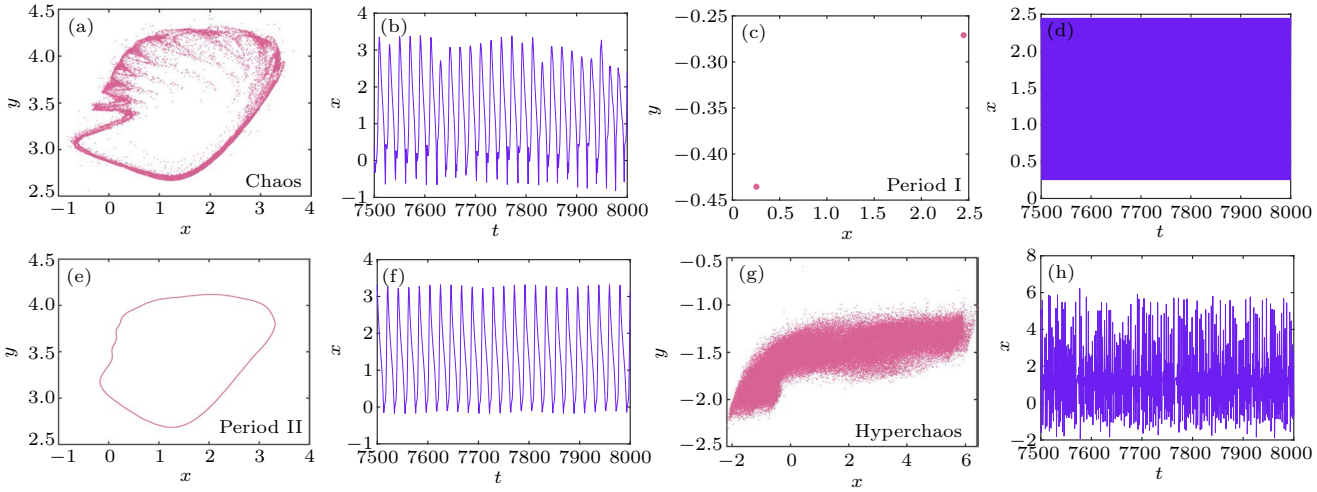


Fig. 10. Phase diagrams and firing models. (a) The phase diagram for $\gamma = -3.03$, (b) the firing pattern for $\gamma = -3.03$, (c) the phase diagram for $\gamma = 2.96$, (d) the firing pattern for $\gamma = 2.96$, (e) the phase diagram for $\gamma = -2.69$, (f) the firing pattern for $\gamma = -2.69$, (g) the phase diagram for $\gamma = 7.18$, (h) the firing pattern for $\gamma = 7.18$.

4.1.3. The variation of neuron parameter μ

To study the effect of the neuronal parameter μ on the R-M-R map, as presented in Fig. 11, the BDs in different planes and LEs when $\mu \in (0.01, 0.6)$ are plotted. The initial values are set to (0.1, 0.1, 0, 0.1, 0, 0), with $\gamma = -4$, $k = 0.1$, $b_1 = 0.1$, $b_2 = 0.1$,

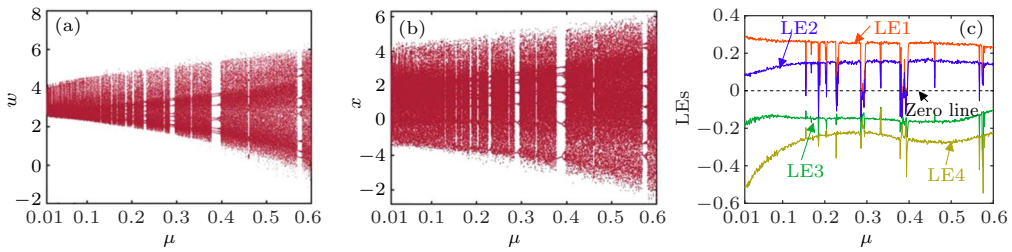


Fig. 11. Dynamical characteristics change with μ. (a) The BD in the μ–w plane, (b) the BD in the μ–x plane, (c) LEs.

$\sigma = 1.35$, $h = 0.11$ are kept unchanged. From the BD and LEs, it can be seen that the map undergoes multiple period-doubling bifurcations with the change of μ, eventually entering a hyperchaotic state, during which multiple periodic windows also exist. Figure 12 shows the typical attractor phase diagrams and corresponding firing patterns.

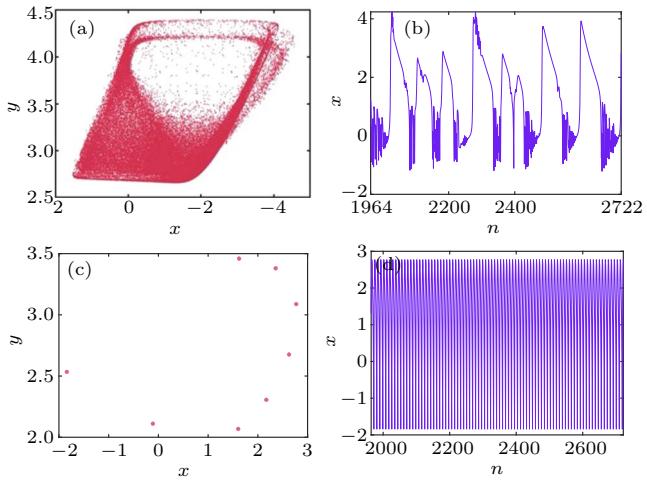


Fig. 12. Phase diagrams and firing models of attractors for different μ. (a) The phase diagram for $\mu = 0.02$, (b) the firing pattern for $\mu = 0.02$, (c) the phase diagram for $\mu = 0.29$, (d) the firing pattern for $\mu = 0.29$.

When $\mu = 0.02$, the map exhibits a hyperchaotic state, and triangular burst firing is observed in the firing pattern. When $\mu = 0.29$, the firing pattern exhibits periodic spike firing.

4.2. Firing patterns

Neurons, as the basic units for information transmission and processing in the brain, have their firing patterns, that is, the temporal patterns and frequency characteristics of electrical signals generated by neurons after receiving input signals and transmitting information. These firing patterns play a crucial role in maintaining the normal functions of the brain and the occurrence and development of brain diseases. The firing process and patterns of discrete neurons can be described by iterative mappings, and with the change of R-M-R mapping parameters, a variety of different firing patterns can be observed. These patterns are inextricably linked to brain diseases.[57–59] Figure 13 shows the change of the firing pattern of the x sequence with the number of iterations n. The initial value is set to $(1,1,0,-1,1,1)$, and the relevant parameters of the firing pattern are listed in Table 3.

Different firing patterns correspond to distinct neural functions. Under normal conditions, as shown in Fig. 13(a), the R-M-R map presents a periodic spike firing pattern. This pattern is a specific type of neuronal firing characterized by fixed temporal rhythms and repeatable spike signals, with "regular repetition" as its core feature. In brain information processing, it undertakes core functions such as "rhythm synchronization", "timing regulation", and "key signal marking". Meanwhile, it also serves as an important marker for various brain functional states, including sleep and cognition, as well as pathological states such as epilepsy.[60]

Figure 13(b) presents the chaotic spike firing pattern, which is a special type of neuronal firing distinct from regular periodic firing: it appears random and disordered, yet actually follows the laws of nonlinear dynamics. Its core feature is "deterministic chaos": although there is no fixed rhythm in the firing interval, frequency, or intensity, the pattern is regulated by clear neurophysiological mechanisms (such as ion channel activity and synaptic connection strength), and slight differences in initial conditions can lead to significant deviations in the firing trajectory. As a key tool for the brain to process "complex, dynamic, and ambiguous information", this pattern is widely involved in advanced brain functions including decision-making, learning, and creative thinking.[61]

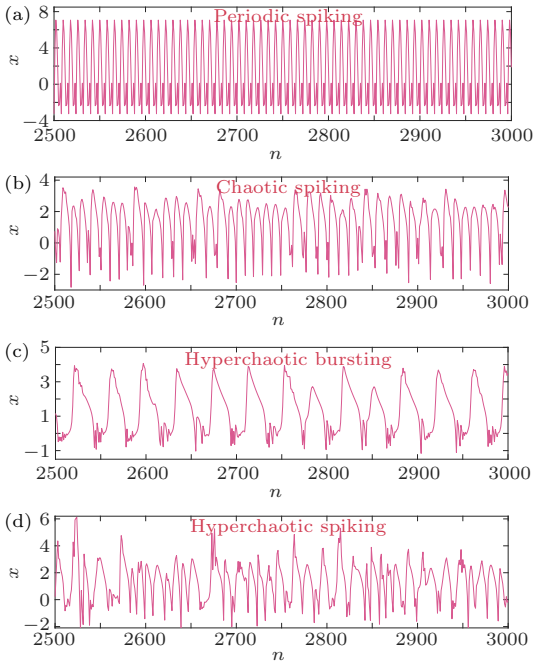


Fig. 13. The firing diagrams of the x-sequence. (a) Periodic spiking, (b) chaotic spiking, (c) hyperchaotic bursting, (d) hyperchaotic spiking.

Table 3. Parameter settings for different firing patterns.

Firing patterns	γ	k	b_1	b_2	μ	σ	h
Periodic	–7	0.02	0.1	0.1	0.66	1.35	0.11
Chaotic	–5.14	0.1	0.1	0.1	0.15	1.35	0.11
Hyperchaotic	–3.67	0.1	0.1	0.1	0.07	1.35	0.11
Hyperchaotic	–4	0.1	3.5	0.1	0.15	1.35	0.11

Figures 13(c) and 13(d) show the firing sequences of two patterns: hyperchaotic bursting firing and hyperchaotic spiking firing. Hyperchaotic bursting firing is characterized by the alternation of "burst clusters and silent periods": during a burst, the signal rises rapidly and then falls, with relatively obvious intervals between clusters. In contrast, hyperchaotic spike firing mainly consists of isolated spikes, which are distributed discretely and have no obvious periodic alternation of "burst-silence". Both patterns embody the core characteristics

of hyperchaotic firing — "deterministic disorder" and multi-dimensional fluctuations — and provide an intuitive reference of firing patterns for understanding the neural mechanisms underlying the brain's processing of complex information.[62]

4.3. Transient chaos and intermittent chaos

When analyzing a system, the situation where its dynamic states change over time from the perspective of the time scale is referred to as the state transition phenomenon. The analysis of this state transition phenomenon holds significant importance in the field of chaotic image encryption. In the coupled Rulkov neuron model, two types of state transition phenomena have been discovered. By setting parameters $b_1 = -1.73$, $\gamma = -4$, $k = 0.1$, $b_2 = 0.1$, $\mu = 0.15$, $\sigma = 1.35$, and $h = 0.11$ and the initial value is (0.1, 0.1, 0, 0.1, 0, 0), the first type of state transition leads to chaotic degradation, where the transient chaotic attractor transforms into a stable periodic state. As shown in Fig. 14(a), the chaotic state occurs when the number of iterations n satisfies $0 < n < 66607$, and the stable periodic state appears when $66607 < n < 80000$. Figure 14(a) shows the chaotic attractor and periodic attractor in the x–y plane. To more clearly display the chaotic and periodic firing patterns, Figs. 14(b) and 14(c) present local enlarged views.

When the parameters are set as $k = -0.019$ and $b_1 = 0.1$ (with other parameters and initial values unchanged), the second type of state transition occurs. The map exhibits periodic states in the time intervals $1000 < n < 1373$, $5854 < n < 6277$, and $8875 < n < 9500$, while it is in hyperchaotic states between $1373 < n < 5854$ and $6227 < n < 8875$. As shown in Fig. 14(b), the complete transition process involves two shifts from periodic states to transient hyperchaotic states, eventually degenerating into a periodic state. The corresponding phase portraits in the x–z plane are also depicted.

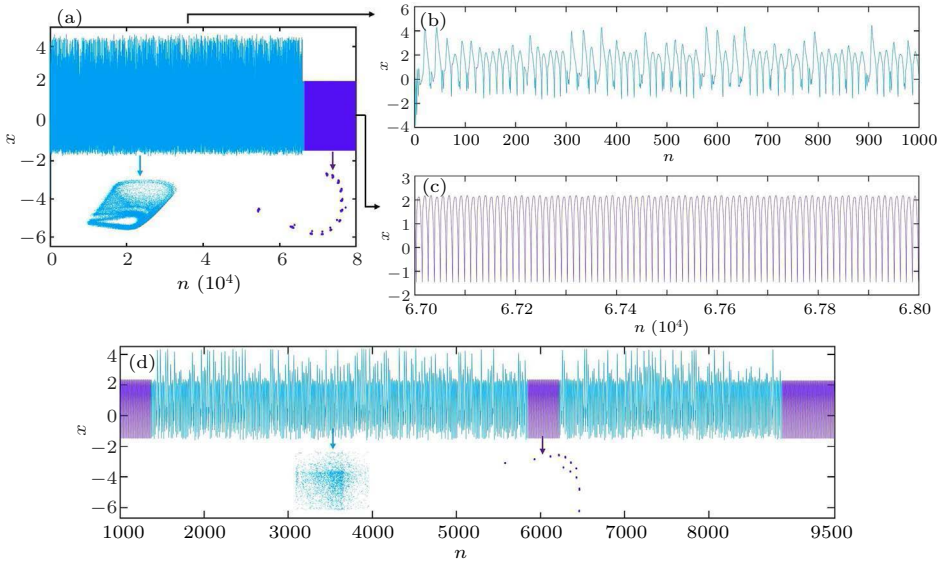


Fig. 14. State transition of the system. (a) Transient chaos, (b) the chaotic sequence with $0 < n < 1000$, (c) the periodic spike firing with $67000 < n < 68000$, (d) intermittent chaos.

4.4. Coexisting attractors

Coexisting attractors refer to the phenomenon where a map converges to different attractors due to different initial values under the same parameter conditions. It reveals the complexity of map behavior and sensitivity to initial values, serving as an important feature of chaotic systems and nonlinear dynamics. This phenomenon can be applied in key scenarios such as neural networks and cryptography. Synaptic crosstalk can change the firing patterns of neurons and affect the synchrony or stability of neural networks. In the neuron model R-M-R map, the intensity of parameter b_1 is a key factor that triggers the coexistence of attractors.

Set the parameters as $\gamma = -3$, $k = 0.1$, $b_2 = 0.1$, $\mu = 0.12$, $\sigma = 1.26$, $h = 0.62$, and the initial values as $(-1, 1.2, 0, 0, -1, 1)$ and $(-2, 1.5, 0, -1, 0, 1)$ respectively. Figures 15(a) and 15(b) show the attractor basin diagrams under different initial conditions. By comparing Figs. 15(a) and 15(b), it can be seen that slight changes in the initial conditions also lead to significant differences in the basin structures. The colors in the figures exhibit striped and fragmented distributions, corresponding to bifurcation and chaotic behaviors, respectively. As b_1 changes, the attractor evolves from a simple cycle into period-doubling bifurcations and finally into chaos, which has a corresponding relationship with the coexisting bifurcation diagram shown in Fig. 15(c) as b_1 changes. To illustrate this more clearly, Fig. 16 presents specific coexisting attractors and corresponding firing diagrams. As shown in Figs. 16(a) and 16(c), small changes in the crosstalk intensity b_1 can lead to the coexistence of two different chaotic attractors. Figure 16(e) demonstrates the coexistence of a chaotic attractor and a periodic attractor when the crosstalk intensity $b_1 = -2.2$.

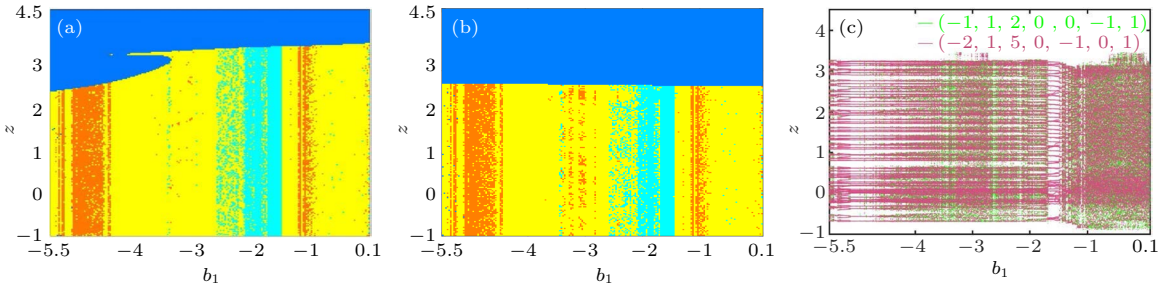


Fig. 15. (a) Attractor basins about the initial value $x_n = -1$, $y_n = 1.2$, $w_n = 0$, $f_n = -1$, $g_n = 1$ and $z_n \in (-1, 4.5)$, $b_1 \in (-5.5, 0.1)$; (b) attractor basins about the initial value $x_n = -2$, $y_n = 1.5$, $w_n = -1$, $f_n = 0$, $g_n = 1$ and $z_n \in (-1, 4.5)$, $b_1 \in (-5.5, 0.1)$; (c) coexisting bifurcation diagram varying with b_1.

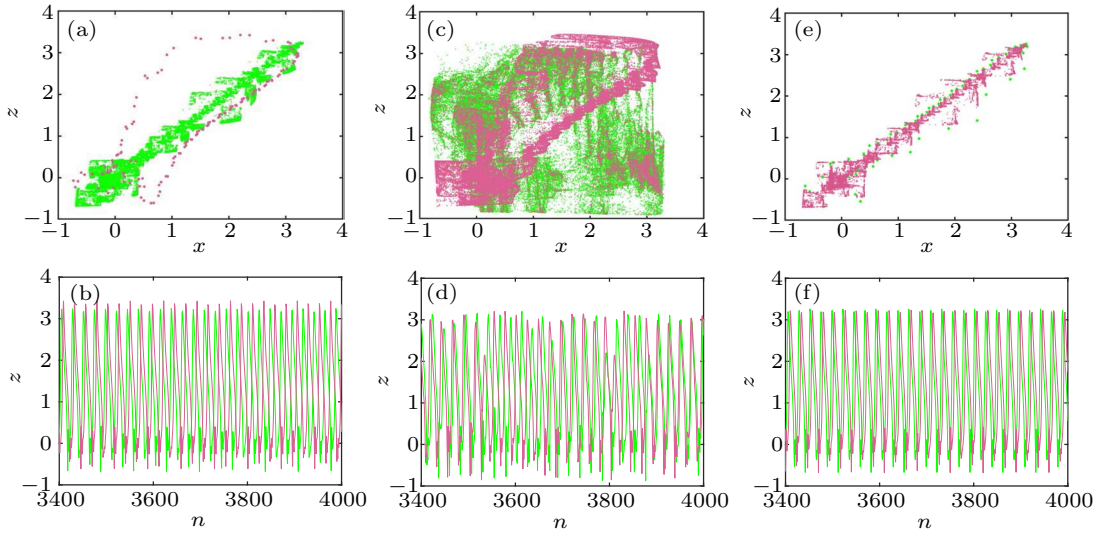


Fig. 16. Coexisting attractors and firing patterns with different b_1 values, pink represents the initial value $(-2, 1.5, 0, -1, 0, 1)$ and green represents $(-1, 1.2, 0, 0, -1, 1)$. (a) x–z plane as $b_1 = -2.8$; (b) firing pattern as $b_1 = -2.8$; (c) x–z plane as $b_1 = -0.3$; (d) firing pattern as $b_1 = -2.8$; (e) x–z plane as $b_1 = -2.2$; (f) firing pattern as $b_1 = -2.2$.

4.5. Complexity analysis

Complexity serves as an effective means to describe the dynamic characteristics of chaotic maps, quantifying the degree of similarity between pseudo-random sequences and truly random sequences. A pseudo-random sequence is a numerical sequence that appears random but is actually generated by deterministic rules, finding extensive applications in fields such as cryptography, communications, and simulation. SE is a method used to analyze the complexity of chaotic systems.

A higher SE value corresponds to greater system complexity, thereby boosting the security of chaotic systems in confidentiality applications. The algorithm flow chart of SE is shown in Fig. 17, where x represents a pseudo-random sequence, N represents the sequence length, $X(K)$ represents the transformed sequence, and $P(K)$ represents the relative power spectral probability. The code for SE complexity is shown in Fig. 18.

Fixing the initial values as (0.1, 0.1, 0, 0.1, 0, 0) and the parameters $b_1 = 0.1$, $k = 0.1$, $\sigma = 0.1$, $b_2 = 1.35$, $h = 0.11$, and varying the neuron control parameters $\gamma \in (-3.1, 2.1)$ and $\mu \in (0.3, 0.6)$, the complexity of the R-M-R map within the γ–μ plane is illustrated in Fig. 19(c). It can be seen that the overall complexity distribution of the R-M-R map is uneven, but the SE can still reach above 0.6. When parameters

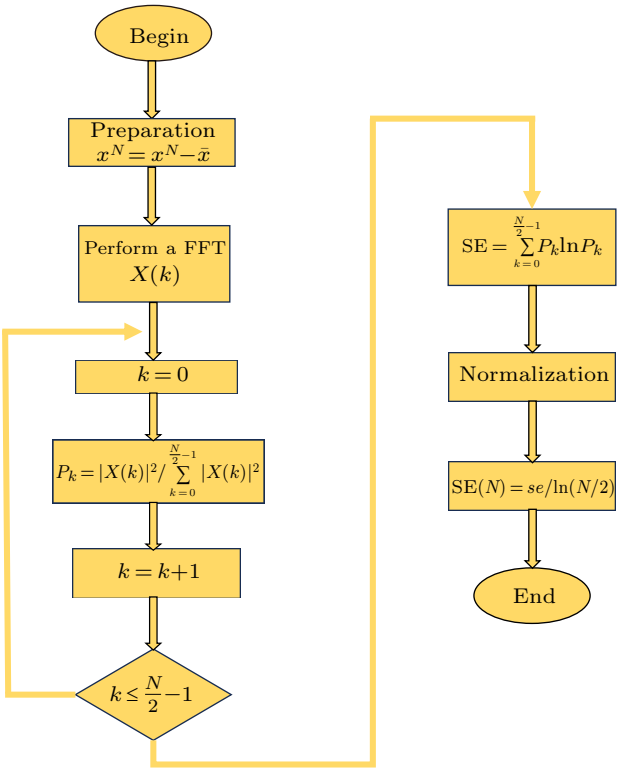


Fig. 17. Flowchart of the SE complexity algorithm.

$h \in (0.4, 0.6)$ and $\mu \in (-0.14, 0.333)$, Fig. 19(d) demonstrates the influence of interaction intensity h and control parameter μ on the R-M-R map complexity.

```
functionSE = SEShannon(x)
N = length(x);
flag = 0;
x = x - mean(x);
fori = 1 : N
if x(i) ~= 0
flag = 1;
end
end
if flag == 0
SE = 0;
return;
end
Y = fft(x);
Xk = (abs(Y).^2). / N;
Xk = Xk(1 : (floor(N / 2)));
ptot = sum(Xk);
PK = Xk. / ptot;
P = 0;
fori = 1 : N / 2
ifPK ~= 0
P = P - PK(i) * log(PK(i));
end
end
se2 = sum(P);
SE = se2 / log(N / 2);
```

Fig. 18. Matlab program of SE complexity code.

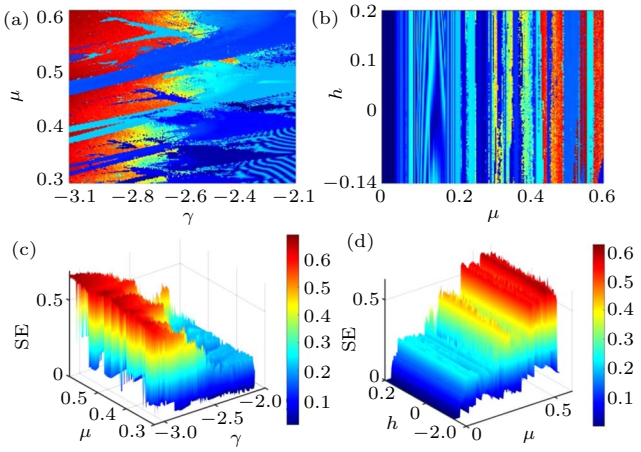


Fig. 19. SE complexity of different parameter planes. (a) 2D complexity diagram in γ–μ plane, (b) 2D complexity diagram in μ–h plane, (c) and (d) the corresponding 3D complexity diagram.

As shown in Fig. 20, when studying the influence of simultaneous changes in initial values and parameters on the complexity of the R-M-R map, it is found that the complexity of the R-M-R map can reach a maximum of 0.8, indicating that the sequence has good pseudo-randomness. In summary, under specific conditions, the newly proposed coupled R-M-R map can generate a high level of complexity, making the sequence more similar to a random sequence.

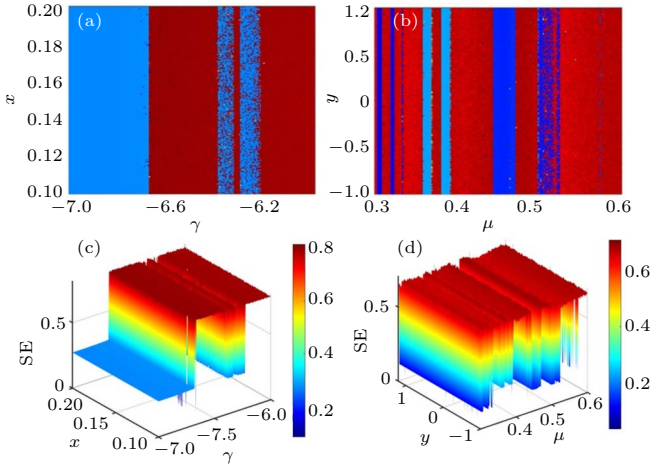


Fig. 20. SE complexity of different parameter planes. (a) 2D complexity diagram in x–γ plane; (b) 2D complexity diagram in y–μ plane; (c) and (d) the corresponding 3D complexity diagram.

5. DSP implementation

For the purpose of observing and testing the results, a modular design scheme is adopted in this paper to illustrate the connections between different components. The hardware interconnection is depicted in Fig. 21(a). As shown in the figure, the TMS320F28335, which interfaces with a computer, is a typical 32-bit floating-point DSP. It is widely used in high-precision control systems and is well-suited for applications in the field of digital signal processing. The DAC8552, featuring 16-bit high resolution, dual-channel, and voltage output, is used in this chip.

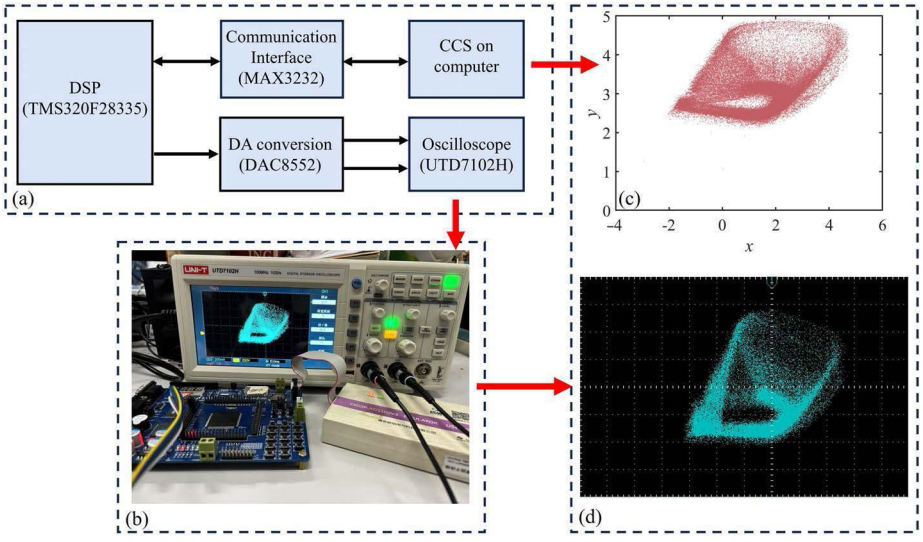


Fig. 21. Circuit structure diagram. (a) DSP hardware implementation, (b) oscilloscope, (c) Matlab platform, (d) chaotic attractor on x–y plane.

Figure 21(b) shows the physical connection. The R-M-R map is initialized with values (0.1, 0.1, 0, 0.1, 0, 0) and parameters $\gamma = -4$, $b_2 = 0.1$, $\mu = 0.15$, $k = 0.1$, $b_1 = 0.1$, $\sigma = 1.35$, and $h = 0.11$. The digital signal processor generates a chaotic sequence, which is first converted into an analog signal. Subsequently, this analog signal is digitized by the DAC and transmitted to the oscilloscope for visualization. Figure 21(d) shows the attractor pattern displayed on the oscilloscope. As depicted in Fig. 21, the modeling outcomes on the DSP platform align with those on the Matlab platform, which proves the feasibility of the map.

6. Conclusion

In this paper, a LAM combined with a sine function is presented, and its non-volatility and local active characteristics are verified through POP and DC V–I plot. The memristor model is then used as a synapse connecting two two-dimensional discrete Rulkov neurons, with synaptic crosstalk introduced between memristors. Through calculation, the equilibrium points of the map are divided into two cases: the first case generates hidden attractors, and the dynamic behavior of the second case is related to parameters. Additionally, nonlinear dynamic analysis methods such as phase diagrams, firing diagrams, BD, LEs and complexity analysis are used to thoroughly explore the dynamic behavioral characteristics of the map. With changes in coupling strength parameters and neuron parameters, states of chaos, hyperchaos, periodic attractors, as well as transient chaos and intermittent chaos are observed. Changing the crosstalk intensity can lead to different types of coexisting phenomena. Furthermore, various firing patterns in the map are identified, including triangular bursting firing, chaotic spiking firing, hyperchaotic spiking firing, hyperchaotic bursting firing, and periodic spiking firing. The complexity reaches a significant magnitude under varying parameters, suggesting that the chaotic sequences derived from this map exhibit strong randomness. Finally, the engineering feasibility of the system is verified on a DSP platform. The constructed neuron model provides a reference for research in artificial intelligence and encryption applications.

Acknowledgements

This work was supported by the National Natural Science Foundation of China (Grant No. 62571079), the Technological Innovation Projects in the Field of Artificial Intelligence in Liaoning Province (Grant No. 2023JH26/10300011), the Basic Scientific Research Projects in the Department of Education of Liaoning Province (Grant No. LJ212410152049), and the Liaoning Provincial Science and Technology Plan Joint Project (Grant No. 2025-BSLH-041).

References

[1] Freeman W J 2000 *Journal of Physiology, Paris* **94** 303
[2] Han B, Zhao F F, Zeng Y and Shen G B 2025 *IEEE Transactions on Pattern Analysis and Machine Intelligence* **47** 240
[3] Yu Z H, Zhu K L, Wang Y and Yang F F 2025 *Chaos, Solitons Fractals* **194** 116233
[4] Boaretto B R R, Manchein C, Prado T L and Lopes S R 2021 *Neural Networks* **137** 97
[5] Ma T, Mou J, Banerjee S and Cao Y H 2023 *Chaos, Solitons Fractals* **176** 114113
[6] Bashkirtseva I, Nasyrova V and Ryashko L 2018 *Communications in Nonlinear Science and Numerical Simulation* **63** 261
[7] Stenzinger R V and Tragtenberg M H R 2025 *Chaos* **35** 013132
[8] Jaimes R R, Huerta C G, García L J H and Pisarchik A N 2022 *Euro. Phys. J. Spec. Top.* **231** 255
[9] Liang H M, Yu Z Y, Jing Z X, Chai Z J and Wang Y X 2024 *Euro. Phys. J. Plus* **139** 241
[10] Yang F F, Ren L J, Ma J and Zhu Z G 2024 *Journal of Zhejiang University-Science A* **25** 382
[11] Xu Q, Wang Y T, Iu H H C, Wang N and Bao H 2023 *IEEE Transactions on Circuits and Systems I-Regular Papers* **70** 3130
[12] Li C B, Li Y X, Yu W N, Irene M and Christos V 2025 *Nonlinear Dyn.* **113** 3857
[13] Leng X X, Wang X P and Zeng Z G 2024 *Chaos, Solitons Fractals* **183** 114944
[14] Lin H R, Wang C H, Deng Q L, Xu C, Deng Z K and Zhou C 2021 *Nonlinear Dyn.* **53** 959
[15] Bertrand Frederick Boui A Boya, Kengne J, Kenmoe G D and Yves J 2022 *Heliyon* **8** e11046
[16] Liu B, Peng X A and Li C L 2024 *AEU-International Journal of Electronics and Communications* **178** 155283
[17] Bao B C, Wang Z W, Hua Z Y, Chen M and Bao H 2023 *Nonlinear Dyn.* **111** 13499
[18] Bao H, Wang Z W, Hua Z Y, Yu X H, Xu Q and Bao B C 2024 *IEEE Transactions on Industrial Informatics* **20** 4784
[19] Ma M L, Xie X H, Yang Y, Li Z J and Sun Y C 2023 *Chin. Phys. B* **32** 058701
[20] Mou J, Ma T, Banerjee S and Zhang Y S 2024 *IEEE Transactions on Circuits and Systems I-Regular Papers* **71** 1771
[21] Bao H, Wang R M, Tang H G, Chen M and Bao B C 2025 *IEEE Internet of Things Journal* **189** 20902
[22] Lu J Y, Xie X H, Lu Y P, Wu Y L, Li C L and Ma M L 2024 *Chin. Phys. B* **33** 048701
[23] Ding D W, Niu Y, Zhang H W, Yang Z L, Wang J, Wang W and Wang M Y 2024 *Chin. Phys. B* **33** 050503
[24] Yu F, He S Q, Yao W, Cai S and Xu Q 2025 *IEEE Transactions on Computer-Aided Design of Integrated Circuits and Systems* **44** 4564
[25] Veletic M and Balasingham I 2020 *IEEE Transactions on Communications* **68** 841
[26] Kim D and Lee J S 2022 *Advanced Functional Materials* **32** 2200497
[27] Yu X H, Bao H, Chen M and Bao B C 2023 *Chaos, Solitons Fractals* **171** 113442
[28] Chua Leon 1971 *IEEE Transactions on Circuit Theory* **18** 507
[29] Shi F, Cao Y H, Banerjee S and Mou J 2025 *Nonlinear Dyn.* **113** 12165
[30] Yu F, Tan B H, He T, He S Q, Huang Y Y, Cai S and Lin H R 2025 *Mathematics* **13** 726
[31] Gao S, Ho C I, Herbert, Erkan U, Simsek C, Toktas A, Cao Y H, Wu R, Mou J, Li Q and Wang C P 2025 *IEEE Transactions on Circuits and Systems for Video Technology* **35** 7706
[32] Wu F Q, Guo Y T, and Ma J 2022 *Nonlinear Dyn.* **109** 2063
[33] Gao S, Ding S Q, Ho C I, Herbert, Erkan U, Toktas A, Simsek C, Wu R, Xu X Y, Cao Y H and Mou J 2025 *Chaos* **35** 073105
[34] Yang F F, Song X L and Yu Z H 2025 *Nonlinear Dyn.* **113** 7213
[35] Yu F, Wu C R, Lin Y, He S Q, Yao W, Cai S and Jin J 2024 *Nonlinear Dyn.* **112** 12393
[36] Hong Q H, Zhao L and Wang X P 2019 *Neurocomputing* **330** 11
[37] Gao S, Zhang Z Y, Li Q, Ding S Q, Iu H H C, Cao Y H, Xu X Y, W C P and Mou J 2025 *IEEE Transactions on Dependable and Secure Computing* **22** 8011
[38] Yu F, Su D, He S Q, Wu Y Y, Zhang S K and Yin H G 2025 *Chin. Phys. B* **34** 050502
[39] Lu Y C, Li H M and Li C L 2023 *Neurocomputing* **544** 126246
[40] Huang L L, Jin P P, Zang H Y, Fu H Y, Lei T F and Wang G Y 2025 *Chaos, Solitons Fractals* **195** 116271

[41] Xu Q, Wang Y T, Wu H G, Chen M and Chen B 2024 *Chaos, Solitons Fractals* **179** 114458

[42] Mou J, Cao H L, Zhou N R and Cao Y H 2024 *IEEE Transactions on Cybernetics* **54** 7333

[43] Li H D and Min F H 2024 *IEEE Transactions on Industrial Informatics* **20** 10259

[44] Li H D and Min F H 2025 *IEEE Transactions on Circuits and Systems I: Regular Papers* **72** 4820

[45] Li H D and Min F H 2025 *IEEE Internet of Things Journal* **12** 29018

[46] Zhang S H, Zhang H L, Wang C and Lin H R 2024 *Chaos, Solitons Fractals* **179** 114459

[47] Li Z, Peng C, Wang M and Ma M 2024 *Indian Journal of Physics* **98** 1043

[48] Qiu R, Dong Y J, Jiang X and Wang G Y 2022 *Electronics* **11** 3034

[49] Shrivastava A N, Triller A and Sieghart W 2011 *Frontiers in Cellular Neuroscience* **5** 7

[50] Zhang S H, Zhang H L, Wang C and Lin H R 2024 *Chaos, Solitons Fractals* **179** 114459

[51] Li Z J, C P, Wang M J and Ma M L 2024 *Indian Journal of Physics* **98** 1043

[52] Lai Q and Yang L 2023 *Chaos, Solitons Fractals* **174** 113807

[53] Rulkov N F 2002 *Phys. Rev. E* **65** 041922

[54] Claudio B, Robert J B, Erol B, Katarzyna J B, Andrzej C, Wilhelmus H I M D, Wolfgang K, Robert T K, Fernando L da S, Paul N, Robert O, Jaeseung J, Roberto Pascual-M, Pedro Valdes-S, Mark H 2020 *Clinical Neurophysiology* **131** 285

[55] Phi L G, William O T, Arielle C and Peter W K 2025 *Clinical Neurophysiology* **171** 76

[56] Pijn J P, Van N J, Noest A and Lopes D S F 1991 *Electroencephalogr Clin Neurophysiol* **79** 371

[57] Shao J, Liu Y H, Gao D S, Tu J and Yang F 2021 *Frontiers in Cellular Neuroscience* **15** 741292

[58] Ni Z G, Bouali B R, Gao D M, Benabid A L and Benazzouz A 2001 *Brain Research* **899** 142

[59] Jia B and Gu H G 2017 *International Journal of Bifurcation and Chaos* **27** 1750113

[60] Farmer D G S, Patros M, Ottaviani M M, Dawood T, Kumric M, Bozic J, Badour M I, Bain A R, Barak O F, Dujic Z and Macefield V G 2025 *Journal of Physiology-London* **603** 1941

[61] Yambe T, Asano E, Mauyama S, Shiraishi Y, Shibata M, Sekine K, Watanabe M, Yamaguchi T, Kuwayama T, Konno S and Nitta S 2005 *Biomedicine & Pharmacotherapy* **59** S236

[62] Fadakar H, Rudra P, Adhikari A, Perera G K, Sirimanne V, Kaur D, Wong H, Yiu K Y, Schweitzer D and Akefe I O 2025 *Neuroscience and Biobehavioral Reviews* **175** 106242